Hydrogen Generation in a Reverse-Flow Microreactor: 1. Model Formulation and Scaling

Niket S. Kaisare and Jay H. Lee
School of Chemical and Biomolecular Engineering, Georgia Institute of Technology, Atlanta, GA 30332

Andrei G. Fedorov
Woodruff School of Mechanical Engineering, Georgia Institute of Technology, Atlanta, GA 30332

DOI 10.1002/aic.10492
Published online May 19, 2005 in Wiley InterScience (www.interscience.wiley.com).

A 1-D model for methane partial oxidation in a tubular microreactor is considered. This work is motivated by a recent report by Kikas et al. that experimentally demonstrated the possibility of autothermal generation of hydrogen by partial oxidation of methane in a tubular microreactor. The reactor consists of four cylindrical channels, each 500 microns in diameter, containing Pt/13%–Rh catalyst. Autothermal generation of hydrogen was possible in both unidirectional (UD) and reverse-flow (RF) operations of the reactor, with the RF operation providing better hydrogen yield and lower temperatures than those of the UD operation. Critical comparison of methane oxidation and reforming kinetics from the literature is performed. An analysis of the timescales of individual processes within the reactor is presented to gain fundamental insight into the reactor operation. Finally, the effect of radiation heat transfer is also considered, and it is found to play an important role for a shorter-size reactor. © 2005 American Institute of Chemical Engineers *AIChE J,* 51: 2254–2264, 2005

Keywords: partial oxidation, reverse-flow reactor, time-scale analysis, radiation, hydrogen for fuel cells

Introduction

Conversion of methane or natural gas to synthesis gas by endothermic steam reforming or autothermal partial oxidation has been investigated extensively.[1] The changing geopolitical situation and the growing need to power emerging civilian, space, or military applications have ensured that hydrogen generation remains an active research area, although the technology, scales of operation, and the end use keep changing. Traditionally, hydrogen is considered a useful raw material for manufacture of ammonia, urea, methanol, and other petrochemical applications. After the energy crisis in the 1970s and more recently the Gulf wars, conversion of synthesis gas to liquid fuels using Fischer–Tropsch synthesis gained significant attention.[2,3] More recently, hydrogen is being used in fuel cells for applications varying from powering portable electronic devices, to providing vehicle motive power, to large-scale power generation.[4]

Two main types of micro fuel cells currently researched as possible replacements for the existing portable energy sources are hydrogen-based fuel cells and direct methanol-based fuel cells. One of the important challenges in making the former a viable technology is the on-demand and energy-efficient generation of hydrogen. Successful commercialization of this technology requires the reactor to run unattended for long periods of time and operate *autothermally*, that is, without external addition of heat. Recently, Fedorov and coworkers[5] experimentally demonstrated the possibility of autothermal reforming of methane in a tubular microreactor, when runs in either unidirectional (UD) or reverse-flow (RF) mode. They showed that running the reactor with periodic reversal of flow direction results in an increase in the hydrogen yield compared to the unidirectional operation. The reactor feed consisted of methane and oxygen at room temperature and Pt wire was used as a catalyst.

The aim of this two-part paper is to develop a one-dimensional (1-D) model that combines heat and mass transfer with heterogeneous catalytic reactions for the reactor of Kikas et al.[5] We first present the formulation of the model equations and selection of reaction kinetics for partial oxidation. Currently, there is no consensus whether the reactions proceed by direct partial oxidation[6] or by indirect oxidation-reforming steps.[7] Herein, the latter reaction chemistry consisting of oxidation, reforming, and water-gas shift reactions is assumed and the

Correspondence concerning this article should be addressed either to J. H. Lee at jay.lee@che.gatech.edu or to A. G. Fedorov at andrei.fedorov@me.gatech.edu.

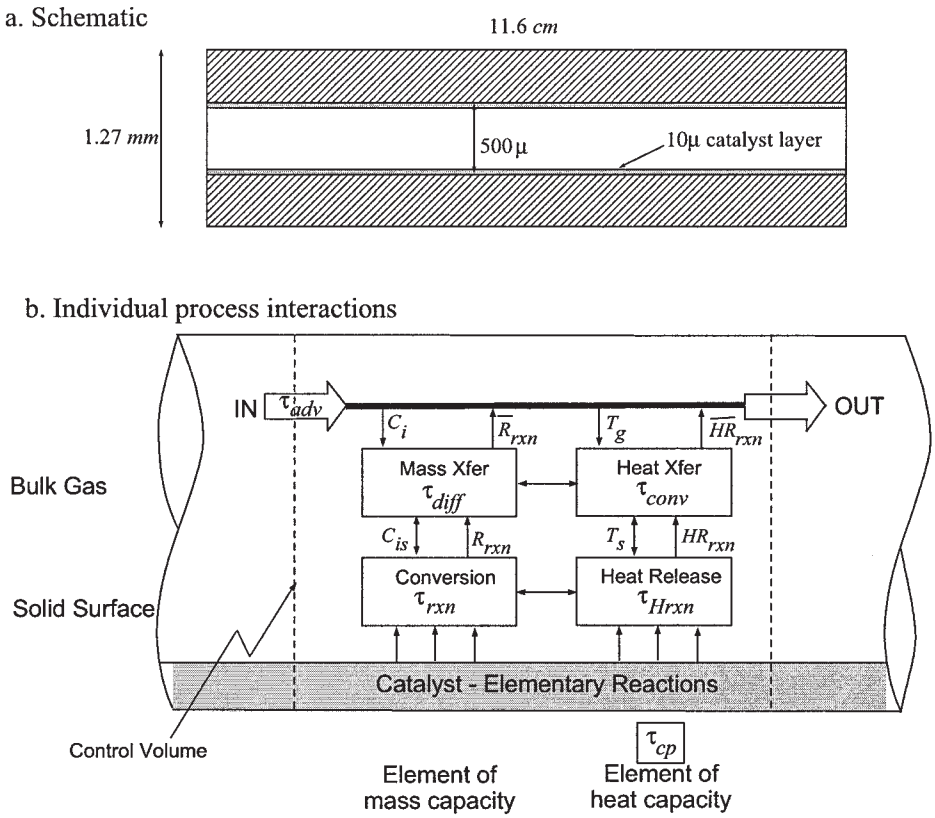

Figure 1. (a) Single channel in the microreactor with its relevant dimensions used for modeling. (b) Interaction of various individual processes within the reactor and their timescales.

kinetic equations developed by Gosiewski et al.[7] are used. The sensitivity to the kinetic equations is demonstrated by comparing the above kinetics with those considered by de Smet et al.[8] The main reaction generating hydrogen is the endothermic reforming reaction ($CH_4 + H_2O \rightleftharpoons CO + 3H_2$, $\Delta H^0_{298} = 206.2$ kJ/mol), which is catalyzed at elevated temperatures and thus requires addition of heat to sustain the reaction. In autothermal operation, this heat is provided by the highly exothermic oxidation of methane ($CH_4 + 2O_2 \rightleftharpoons CO_2 + 2H_2O$, $\Delta H^0_{298} = -802.3$ kJ/mol). Because the overall global reaction occurring in the reactor ($CH_4 + 0.5\ O_2 \rightleftharpoons CO + 2H_2$, $\Delta H^0_{298} = -35.7$ kJ/mol) is only slightly exothermic, reverse flow reactors have been used to maintain autothermal operation of the reactors by using the catalyst bed as a regenerative heat exchanger.[9,10]

The comparison of UD and RF operations of the reactor is the main focus of this study. Blanks et al.[9] provided one of the first experimental and simulation studies of autothermal methane partial oxidation in a pilot-scale fixed-bed reverse-flow reactor (RFR). Later, de Groote et al.[10] and Gosiewski et al.[7] performed simulation studies of methane partial oxidation in a fixed-bed RFR. In both cases, a thermal wave with moving reaction zone was observed in the UD operation; thus the RF operation was required to trap the thermal wave within the reactor and maintain autothermal operation. This study differs from the above-mentioned papers on two accounts. First, because the reactor is a microchannel reactor, reagents need to diffuse over a shorter distance. The reactions may therefore proceed close to their intrinsic rates. The catalyst loading in this reactor is significantly lower than that in a fixed-bed reactor because the catalyst is not in a well-dispersed state. Second, autothermal operation was possible in the microreactor for both the UD and RF operations. To our knowledge, this is the first study on the comparison of the UD and RF operations of methane partial oxidation in a microreactor. Further, a review of the literature indicates that radiation heat transfer has largely been neglected in previously reported simulations of partial oxidation. Therefore, we devote the last section of this paper to modeling the effect of radiation heat transfer. We demonstrate that in spite of high emissive power in the reactor, the overall effect of radiation is marginal in the longer reactor with high aspect ratio ($l/d = 232$). However, the effect of radiation on a shorter reactor ($l/d = 100$) is quite significant.

Reactor Model

Description and model equations

The experimental reactor of Kikas et al.[5] consists of a ceramic tube with four cylindrical channels (500 microns ID; 11.6 cm length). The center of each reactor channel contains Pt/13%–Rh wire that acts as a catalyst. The ceramic tube is housed in a steel casing with heating elements wrapped around it, which are used to ignite the partial oxidation reactions during reactor start-up. The entire setup is insulated to minimize the heat losses. We attempt to analyze numerically these experiments to develop an insight into the advantage offered by RF operation observed in experiments.[5] We model an equivalent single tube of the reactor, as shown in Figure 1a.

To this end, a one-dimensional (1-D), two-phase model is

developed for simulating the autothermal operation of the reactor. The process properties (temperatures, concentrations, etc.) are assumed to be uniform in cross-sectional directions. The flow is one dimensional and laminar, and the reactants and products are assumed to be ideal gases. Heterogeneous reaction chemistry consisting of oxidation, reforming, and water-gas shift reactions is considered. The pseudo-steady-state assumption is used for the species balance on solid surface.

The resulting conservation equations for species and energy are as follows

$$\frac{\partial}{\partial t} C_i + \frac{\partial}{\partial z} vC_i = -k_{gi}\hat{a}(C_i - C_{is}) \tag{1}$$

$$0 = k_{gi}(C_i - C_{is}) + \sum_{j=1}^{n_{rxn}} \nu_{ij} r_j \tag{2}$$

$$\frac{\partial}{\partial t} T_g + v \frac{\partial}{\partial z} T_g = \frac{h_v \hat{a}}{\rho_g c_{pg}} (T_s - T_g) + \frac{(1-\alpha)\hat{a}}{\rho_g c_{pg}} \sum_{j=1}^{n_{rxn}} (-\Delta H_j) r_j \tag{3}$$

$$\frac{\partial}{\partial t} T_s = \frac{\lambda_s}{\rho_s c_s} \frac{\partial^2}{\partial z^2} T_s - \frac{h_v \underline{a}}{\rho_s c_s} (T_s - T_g) + \frac{\underline{a}}{\rho_s c_s} \left\{ \alpha \sum_{j=1}^{n_{rxn}} (-\Delta H_j) r_j - q_r - q_\infty \right\} \tag{4}$$

In the full three-dimensional (3-D) model, the reaction heat term would appear as a boundary condition. For 1-D models, it is customary to attribute the heat of reaction to the solid heat balance (that is, $\alpha = 1$). However, for the sake of generality, we consider splitting the heat of reaction term between the solid and gas phases in Eqs. 3 and 4 through the parameter α taking a value between 0 and 1. The radiation effects (q_r) are neglected at first, and included in the analysis in the last section of this paper. The effect of heat loss (q_∞) is not considered herein, but is analyzed in the companion study.[11]

The mass- and heat-transfer coefficients are computed using the Nusselt (Nu) and Sherwood (Sh) number correlations for fully developed laminar flow in cylindrical channels, based on constant heat flux and surface concentration boundary conditions, respectively

$$N_{\mathrm{Nu}} = \frac{h_v d}{\lambda_g} = 4.36 \qquad N_{\mathrm{Sh}} = \frac{k_{gi} d}{\mathcal{D}_i} = 3.66$$

The pertinent boundary conditions are as follows

$$C_i(0, t) = C_{i0}$$

$$T_g(0, t) = T_{g0}$$

$$\lambda \left.\frac{\partial T_s}{\partial z}\right|_{0,t} = h_{in}[T_s(0, t) - T_{g0}] + \varepsilon\sigma[T_s^4(0, t) - T_{g0}^4]$$

Table 1. Nominal Operating Conditions for Simulations

Reactor length	l	11.6 cm
Channel diameter	d	500 μ
Ceramic tube OD	d_t	0.254 cm
Number of channels		4
Inlet temperature	T_{g0}	300 K
Inlet velocity	v_0	1.68 m/s
Feed compositions		
$y_{\mathrm{CH_4}}$		0.5
$y_{\mathrm{O_2}}$		0.5
y_i		10^{-8} to 10^{-5}
Preheat temperature	T_{init}	1173 K
Switching time	$\tau_{c/2}$	5 s

$$\left.\frac{\partial T_s}{\partial z}\right|_{l,t} = 0$$

The mole fractions of methane and oxygen are obtained from the feed ratio (0.7 to 1.2) used in the experiments.[5] All other species are assumed to be present in very small quantities to prevent singularities in numerical computations becauses some of them appear as denominators in reaction rates. As an initial condition, the reactor is assumed to be preheated to T_{init} = 1173 K. The nominal operating conditions are summarized in Table 1.

During the RF operation, the input and output ports of the reactor are switched periodically. In computations, the same governing equations and boundary conditions apply in forward and reverse directions. The states are switched according to

$$\phi(z, m\tau^+) = \phi(l - z, m\tau^-) \tag{5}$$

where $\phi(z, t)$ represents any state variable, τ is the half-cycle period, m is an integer index, and the superscripts + and − represent the time after and before switching.

Computing velocity and pressure fields

To solve the model Eqs. 1–4, the velocity field needs to be computed, which is typically done by solving the momentum conservation equation simultaneously with the mass and energy conservation. The 1-D momentum conservation equation is given by

$$\frac{\partial}{\partial t} \rho v + \frac{\partial}{\partial z} \rho v v = -\frac{\partial p}{\partial z} + \mu \frac{\partial^2 v}{\partial z^2} \tag{6}$$

where the ideal gas assumption yields

$$p = \sum_{i=1}^{n_{sp}} C_i R T_g \tag{7}$$

Simultaneously solving Eqs. 1–4 and 6 is computationally very demanding. As a result, one often resorts to making certain assumptions regarding the velocity field.

One possible assumption is to consider the velocity to be constant along the length of the reactor.[17] In reality, for a compressible fluid under quasi steady-state conditions, the total

Table 2. Reaction Kinetics of Gosiewski et al.[7] *

Reaction	Rate of Reaction (mol m^{-2} s^{-1})
Oxidation	$r_1 = 23.06 \exp\left(\frac{-100{,}320}{RT}\right) C_{CH_4} C_{O_2}$
Reforming	$r_2 = 76.16 \exp\left(\frac{-114{,}120}{RT}\right) C_{CH_4} C_{H_2O} \left(1 - \prod_i^{n_{sp}} p_i^{\nu_{i,2}} / K_{eq,2}\right)$
Water-gas shift	$r_3 = 0.412 \exp\left(\frac{-38{,}130}{RT}\right) C_{CO} C_{H_2O} \left(1 - \prod_i^{n_{sp}} p_i^{\nu_{i,3}} / K_{eq,3}\right)$

*This model is denoted as "GOS." All concentrations are in mol/m^3 and pressures are in bar.

mass flux remains constant within the reactor. The increasing temperature and species generation by reaction affects the density of the system, which consequently changes the velocity through the continuity equation. As a result, constant velocity assumption may lead to incorrect results.

Another possibility is to use an empirical pressure drop relationship to specify the pressure field within the reactor and then obtain the velocity field using the overall continuity equation.[10] For laminar flow of gases in cylindrical channels, the pressure drop along the reactor length is $<1\%$ of the total pressure. Indeed, simultaneously solving the energy, mass, and momentum conservation (Eqs. 1–4 and 6) revealed that the pressure drop along the length of the reactor is <0.1 to 0.5% of the total pressure. Thus, it is reasonable to make an assumption that the pressure is constant along the reactor. Summing the species balance (Eq. 1) over all species and neglecting the time-dependent term attributed to very fast mass equilibrium (see timescale analysis in the next section), we obtain the relationship for the change in molar flow rate arising from the reaction[10] as

$$\frac{\partial F}{\partial z} = -\sum_{i=1}^{n_{sp}} k_{gi} \hat{a} (C_i - C_{is}) \tag{8}$$

Coupling Eq. 8 with Eqs. 1–4 and noting that the molar flow rate F (mol m^{-2} s^{-1}) is given by

$$F = v \frac{p}{RT_g} \tag{9}$$

the problem formulation becomes complete.

We found that indeed solving Eqs. 1–4 with Eq. 8 gives accurate results, while requiring much lesser computational time. Thus, in the following discussion, we use the constant pressure assumption and use the continuity Eq. 8 to obtain the velocity within the microreactor.

Reaction kinetics

The indirect partial oxidation of methane is considered to take place through the following three reactions[7,8] on the catalyst surface:

$$CH_4 + 2O_2 \rightarrow CO_2 + 2H_2O \qquad \Delta H^0 = -802.0 \text{ KJ/mol} \tag{10}$$

$$CH_4 + H_2O \rightleftharpoons CO + 3H_2 \qquad \Delta H^0 = +206.1 \text{ KJ/mol} \tag{11}$$

$$CO + H_2O \rightleftharpoons CO_2 + H_2 \qquad \Delta H^0 = -41.15 \text{ KJ/mol} \tag{12}$$

The other reactions that possibly occur in the system, such as CO_2 reforming, CO oxidation, methane reforming to CO_2, and the like. are neglected.

The first set of kinetic equations we consider were developed by Gosiewski et al.[7] for methane partial oxidation and were expressed per kilogram of catalyst for a dispersed Pt on porous alumina pellets. The catalyst loading in the microreactor[5] was computed to be 28.9 mg Pt per channel. However, the catalyst in the microreactor was not dispersed; instead a wire was used. Because the catalyst fraction available for the reactants was not known, the following procedure was used to modify the kinetic rate expressions to account for this fact. We converted the kinetic equations to per square meter catalyst surface basis. We then noted that the density of catalyst particle for the fixed bed system was 2130 kg/m^3, whereas the density of catalyst wire for our microreactor was 19,640 kg/m^3. Thus, we multiplied all the kinetic rate constants by a factor of 9.22, which is equal to the density ratio. The resulting kinetic equations are summarized in Table 2. Hereafter, we will call these kinetic equations the *GOS model*.

The effect of the choice of kinetic equations was also considered. Recently, de Smet et al.[8] compared the reforming kinetics of Xu and Froment[12] (denoted by XF) with those of Numaguchi and Kikuchi[13] (denoted by NK) for indirect partial oxidation of methane. They used the oxidation kinetics of Trimm and Lam[14] for both cases. In this paper, the GOS model is compared with the NK model. The XF model could not be used for the following reason. In the XF model, the rate of reforming reaction has the form

$$r = \frac{k}{p_{H_2}^{2.5}} \frac{p_{CH_4} p_{H_2O} - p_{H_2}^3 p_{CO} / K_{eq}}{\text{den}}$$

where the denominator (den) is given by

$$\text{den} = (1 + K_{CO} p_{CO} + K_{H_2} p_{H_2} + K_{CH_4} p_{CH_4} + K_{H_2O} p_{H_2O} / p_{H_2})^2$$

Table 3. Reaction Kinetics Represented as "NK" in de Smet et al.[8] Combining Oxidation[14] and Reforming[13] Kinetics from Different Sources*

Reaction	Rate of Reaction (mol m^{-2} s^{-1})
Oxidation	$r_1 = 157.7 \exp\left(\frac{-75{,}500}{RT}\right) \frac{p_{CH_4} p_{O_2}}{(1 + K_{CH_4} p_{CH_4} + K_{O_2} p_{O_2})}$
	$K_{CH_4} = 2.28 \times 10^{-3} \exp\left(\frac{25{,}100}{RT}\right) \quad K_{O_2} = 6.41 \times 10^{-4} \exp\left(\frac{45{,}900}{RT}\right)$
Reforming	$r_2 = 72.8 \exp\left(\frac{-106{,}900}{RT}\right) \frac{p_{CH_4} - p_{CO} p_{H_2}^3 / (K_{eq,2} p_{H_2O})}{(K_{sat} + p_{H_2O})^{0.596}}$
Water-gas shift	$r_3 = 0.068 \exp\left(\frac{-54{,}500}{RT}\right)\left(p_{CO} - \frac{p_{CO_2} p_{H_2}}{K_{eq,3}(K_{sat} + p_{H_2O})}\right)$

*All pressures are in bar.

Because the system contains no hydrogen or water in the inlet, this model is not applicable; even with 2% hydrogen and water present in the feed, negative values of p_{H_2O} were predicted. In the NK model, on the other hand, the rate of reforming reaction has an inverse dependency on p_{H_2O}. As a result, at higher CH_4:O_2 ratios, the reforming rate is nonzero even at zero H_2O concentrations. Thus, a "saturation" term was added to the denominator to ensure that the rate approaches 0 as $p_{H_2O} \rightarrow 0$. The value of K_{sat} was taken to be 10^{-4} bar. Another modification was that instead of oxidation kinetics for Pt on porous alumina, the kinetics published for the nonporous catalyst[14] was used. The procedure suggested by de Smet et al.[8] was followed to obtain rate expressions shown in Table 3. In these expressions, the equilibrium constant is computed using the standard thermodynamic relationship

$$\Delta G_j = -RT_s \ln(K_{eq,j}) \tag{13}$$

Solution method and validation

The control volume method with a nonuniform staggered grid was used to discretize the model equations in the spatial domain to obtain a system of differential algebraic equations (DAE). A standard DAE solver called DASPK[15] was used to integrate the resulting DAE system. DASPK uses a fully implicit fifth-order backward difference formula (BDF) with adaptive step size to solve the DAE system. The velocities were computed at grid boundaries and the other variables were computed at nodes (that is, grid centers). The grid was chosen to be symmetric about the center of the reactor, with the grid boundaries lying at $(l/2)[i/\text{int}(N/2)]^{\gamma}$, for $i = 1$ to $N/2$, starting at either ends of the reactor. For the value of $\gamma = 1.0$, a uniformly spaced grid is obtained. A grid-independence study was performed with the γ-value ranging between 1.0 and 2.0, and the optimum values of $\gamma = 1.2$ and $N = 175$ were obtained for good accuracy and a reasonable speed of computation.

During simulations, absolute and relative errors of 10^{-5} were used for all variables. The consistency of the converged results was checked by computing the residuals of the mass and energy balance equations and verifying that they were less than the desired error tolerance. Before using the code for simulation of this system, it was tested against some standard examples. Specifically, a standard heat conduction problem and a standard heat transfer problem with first-order reaction (with $T_g = T_s$) were solved by making minimum changes to the codes. Satisfactory agreement was obtained between simulations and analytical solutions for standard problem.[16]

Timescale Analysis

Consider a small volume element within the reactor. Figure 1 shows the interactions between various individual processes occurring within this element. The material and energy enter and exit this element by advection; transfer of species occurs from the bulk gas to the catalyst surface by convection and vice versa; several reactions occur on the surface of the catalyst; these reactions result in a net release or consumption of heat; and there is also heat exchange between the solid and the bulk gas. Each of these processes is associated with its own timescale. In addition, the thermal capacity of the reactor is also associated with an "inertial " timescale of thermal relaxation. A *timescale* is defined as "the time required for an individual process to occur assuming that all other processes do not affect the reactor performance."

The timescales of various processes are listed in Table 4. Naturally, the timescales are computed at the locations where their effect is the highest; that is, at or near the reactor hot spot where the reaction rates are the highest. These conditions were obtained from the simulation results for the nominal case, presented in the next section. The reaction timescale was numerically computed as the time required for the reaction to reach equilibrium (or complete conversion for oxidation), starting at concentrations and temperature existing in the bulk gas. The timescale of heat release was computed as shown in Matros[18] by linearizing the reaction heat source term

$$\frac{dT_s}{dt} = \frac{a}{\rho_s c_s} \sum_{j=1}^{n_{rxn}} (-\Delta H_j) r_j(C, T_s)$$

Table 4. Timescales of Various Processes within the Microreactor

Process	Timescale	Value (s)
Advection	$\tau_{ad} = l/v$	0.013
Diffusion	$\tau_{diff} = (k_g a)^{-1}$	0.00014
Oxidation	τ_{ox}, numerical	0.002
Reforming	τ_{ref}, numerical	0.008
Water-gas shift	τ_{wgs}, numerical	0.006
Reaction heat	Eq. 14	3.2
Thermal inertia	τ_{th}, numerical	168

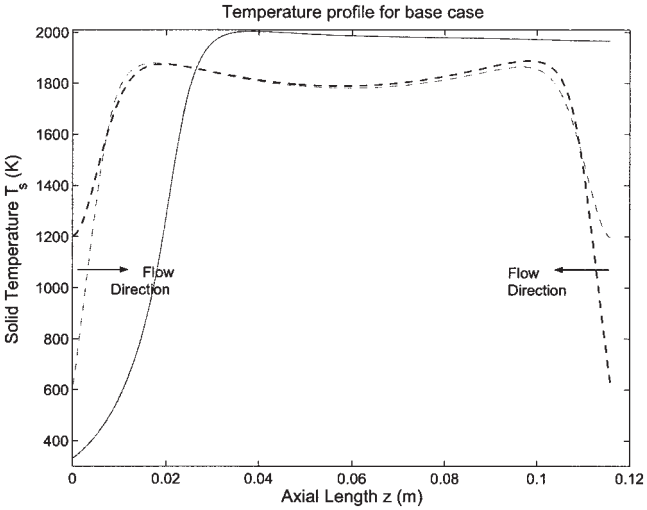

Figure 2. Temperature profiles at the UD steady state and just before flow reversal in RF (at $t = n\tau_{c/2}$) for the GOS model.

The temperature profile is more uniform and the peak lower in the RF operation.

resulting in

$$\tau_{Hrxn} = \frac{\rho_s c_s}{a}\left[\sum_{j=1}^{n_{rxn}}\left(\frac{E_j}{RT_s^2}\right)(-\Delta H_j)r_j(C, T_s)\right]^{-1} \qquad (14)$$

For a single reaction j, it is the time required for the solid temperature to increase by the value RT_s^2/E_j arising from heat release.[18] The overall timescale of heat release, τ_{Hrxn}, is the combined effect attributed to various reactions concurrently taking place within the system.

The timescale of thermal relaxation was also calculated numerically. The system was simulated assuming no reaction, radiation, or heat losses. The energy balance equations for the solid and gas phases were solved simultaneously with $T_s(z, t = 0) = 1173$ K and $T_g(0, t) = 300$ K. The τ_{th} is the time taken for the temperature of an element in the interior of the reactor to drop from $T_s = 1130$ K (5% of the temperature difference) to 343 K (95% of the temperature difference). Note that τ_{th} is the response time of a single volume element in the reactor, which is much less than the time it takes for the reactor to reach steady state.

The simple timescale analysis can give some very important information about the system. First, the timescale of diffusion is smaller than that of the reactions, meaning that the reactions occur at their intrinsic rates. Further, because the timescale for advection is higher than that of all the other reactions, the reactions reach their equilibrium (quasi steady state), and the overall thermal effects within the system are critical in defining the reactor operation in UD or RF modes.

Analysis of Reaction Kinetics

In this section, the simulation of the reactor in UD and RF operations using the GOS and NK models is compared. The axial variations in the velocity are incorporated using the constant pressure assumption as discussed in the previous section. The operating conditions for the simulation of the "baseline case" are taken from those reported in the experiments,[5] and are summarized in Table 1.

Unidirectional and reverse-flow operations: GOS model

We first consider the comparison of UD and RF operations of the adiabatic reactor for the GOS model. Figure 2 shows the temperature profiles in the reactor. In the UD operation, the temperature reaches a maximum in the middle of the reactor, where highly exothermic oxidation dominates. A stable, autothermal steady state is obtained for UD operation of the reactor. For feed ratio of CH_4:O_2 = 1:1, inlet velocity of $v_0 = 1.68$ m/s, and inlet gas temperature $T_{g0} = 300$ K, the maximum temperature reached was 2008 K and the hydrogen yield at steady state was 71.1%.

In the RF operation with a 5-s flow reversal time (the period used in experiments), the temperature peak is attained closer to the reactor ends (Figure 2). The central section of the reactor is maintained at a more uniform temperature, with a sharp drop in the temperature at the reactor end. The widening of the high temperature region also results in a lower temperature peak. The sharp temperature drop at the end of the reactor favors water-gas shift reaction, resulting in an improvement in hydrogen yield. Figure 3 shows the mole fractions of all the species in RF operation after attainment of a periodic steady state, just before switching of the flow direction. Table 5 shows the comparison between UD and RF operations. The GOS model predicts a 2.3% improvement in the hydrogen yield and a 120 K decrease in the peak temperature for CH_4:O_2 = 1:1 and a 4.2% increase in the yield for CH_4:O_2 = 0.7:1. These values are consistent with those reported in the experiments.[5]

Simulation using the NK model

The effect of kinetic rate equations was considered by simulation of indirect partial oxidation using the NK model (see Table 3). The simulation results using this model are compared

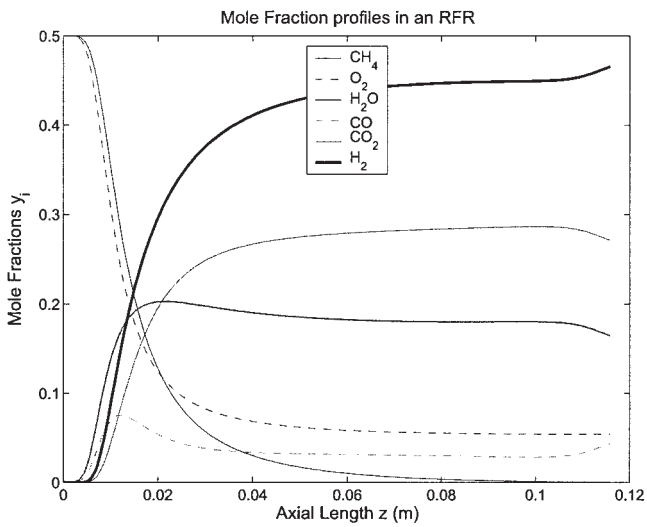

Figure 3. Mole fractions of various species in gas phase just before flow reversal (at $t = n\tau_{c/2}$) in the RF operation with $\tau_{c/2} = 5$ s flow reversal time.

Table 5. Reactor Performance for Experimental Conditions[5] with GOS and NK Kinetics*

		Unidirectional		Reverse Flow		
Model	CH_4:O_2 Ratio	$T_{s,max}$	%H_2 Yield	$T_{s,max}$	$T_{s,out}$	%H_2 Yield
GOS	0.7:1	2160	57.3	2023	1280	61.5
GOS	1:1	2008	71.1	1880	1191	73.4
NK	0.7:1	2561	57.8	2479	1648	58.2
NK	1:1	2308	75.3	2207	1421	74.9

*The experimentally observed trends are matched by the GOS model but not by the NK model.

with those from the GOS model. The results of UD and RF operations are shown in Table 5. The maximum temperature reached in this case was well over 2300 K. This is significantly higher than that predicted by the GOS model because of the low rates of endothermic reforming reactions in the NK model. Increasing the rate of reforming reactions (to assess the sensitivity of the results) by a factor of 1.5 resulted in the disappearance of the autothermal steady state in the UD operation. Moreover, the RF operation did not result in an increase in hydrogen yield over the UD operation, even for CH_4:O_2 = 0.7:1. Thus, this model was unable to predict the experimentally observed behavior of the microreactor.[5] Varying the reaction rates within an order of magnitude (by a factor of 10) did not predict the observed behavior either. This is because the rate of water-gas shift reaction is significantly lower in this model. The shift reaction is thermodynamically favored at low temperatures that exist in the RF operation at the reactor exit. The exit temperatures in the NK model are still quite high. The rate of water-gas shift reaction is significantly lower than that in the GOS model. Thus, no difference between the UD and RF operations was observed for the NK model.

Effect of Radiation

At high temperatures such as those observed in this system, heat transfer by radiation becomes comparable to—or even dominant over—heat transfer by conduction or convection, attributed to the fourth-order dependency of the radiative heat flux on the temperature. In addition to this nonlinear dependency on temperature, radiation heat transfer in a nonparticipating medium is a long-range phenomenon and has complex dependency on properties of the medium and the reactor surface. Thus, incorporating radiation involves solving highly nonlinear integro-differential equations. As a result, radiation has often been ignored in the literature dealing with partial oxidation/reforming.

With a conservative estimate of solid temperature of 1500 K, the radiation to conduction heat-transfer parameter ($N_{rad} = \varepsilon\sigma T^3 d/\lambda$)[19] takes the value of 0.65, indicating that the radiative heat transfer is comparable to solid conduction. In this section, we evaluate the effects of radiation using the net radiosity method[19] to compute the radiation flux within the reactor. We make an assumption that the walls are diffuse gray emitters and reflectors of radiation, and that the medium is essentially transparent (that is, nonparticipating) because of the small channel diameters. All the results reported here are for reactor wall emissivity of $\varepsilon = 0.8$.

For channels with a high aspect ratio (in our system l/d = 232), the finite-difference version of the net radiosity equation can be used instead of the Fredholm integral equation.[20] The finite-difference version matches well with the spatial discretization used in solving the other conservation equations. The outgoing (leaving the wall) radiation flux at any point z_n within the reactor channel is given by

$$q_r(z_n) = \sum_{m=0}^{N} (1-\varepsilon) q_r(z_m) F_{n-m} + \varepsilon \left[E_b(z_n) - \sum_{m=0}^{N} E_b(z_m) F_{n-m} - \sigma T_{in}^4 F_{re}(z_n) - \sigma T_{out}^4 F_{re}(l - z_n) \right] \quad (15)$$

where F_{n-m} is the ring-to-ring view factor and F_{re} is the ring-to-end view factor. The finite view factors are derived using a procedure similar to that presented by Rankin et al.[17] and is given in the Appendix.

Figure 4 compares the solid temperatures in the system with and without radiation accounted for. For the reactor with high aspect ratio, the effect of radiation is not significant. The figure shows that the peak temperature is shifted toward the reactor inlet by about two diameters, which for the simulated system is $<1\%$ of the reactor length. The inset shows a zoom-in plot near the temperature peak. The abscissa for this plot is normalized length, which clearly shows an upstream shift of about two diameters in T_s. These results are consistent with the published literature[20,21], where the temperature curve shifts upstream by one to two diameters. Moreover, the heat loss resulting from radiation at the reactor outlet causes a drop in the temperature at the outlet.

Although the total black body emissive power $E_b(z) = \sigma T_s(z)^4$ is high (same order of magnitude as that of convection flux), radiation does not seem to have a marked effect. The reason for such behavior can easily be seen in the view factor plot in Figure 5. The ring–ring view factor, which determines what fraction of total radiation emitted by a ring element is incident on another surface ring element, diminishes to 0 rapidly near the reactor hot spot. Almost 70% of the radiation emitted by a differential ring element of the reactor is incident on itself. Thus, the computed radiation flux (Figure 6) is two orders of magnitude less than the heat release by reaction and the convective flux.

Finally, the effect of radiation on the shorter (5 cm long) reactor was also studied. The reactor length of 5 cm was chosen to give an aspect ratio of $l/d = 100$. The temperature and mole fractions of hydrogen obtained in this reactor are shown in Figure 7. Again, there is a two-diameter shift in the temperature profile. This is in agreement with Fu et al.,[21] who observed a significant effect of radiation at temperatures lower than those in our system, in their reactor with an aspect ratio of $l/d < 10$. As in the longer reactor, we observed a drop in the temperature

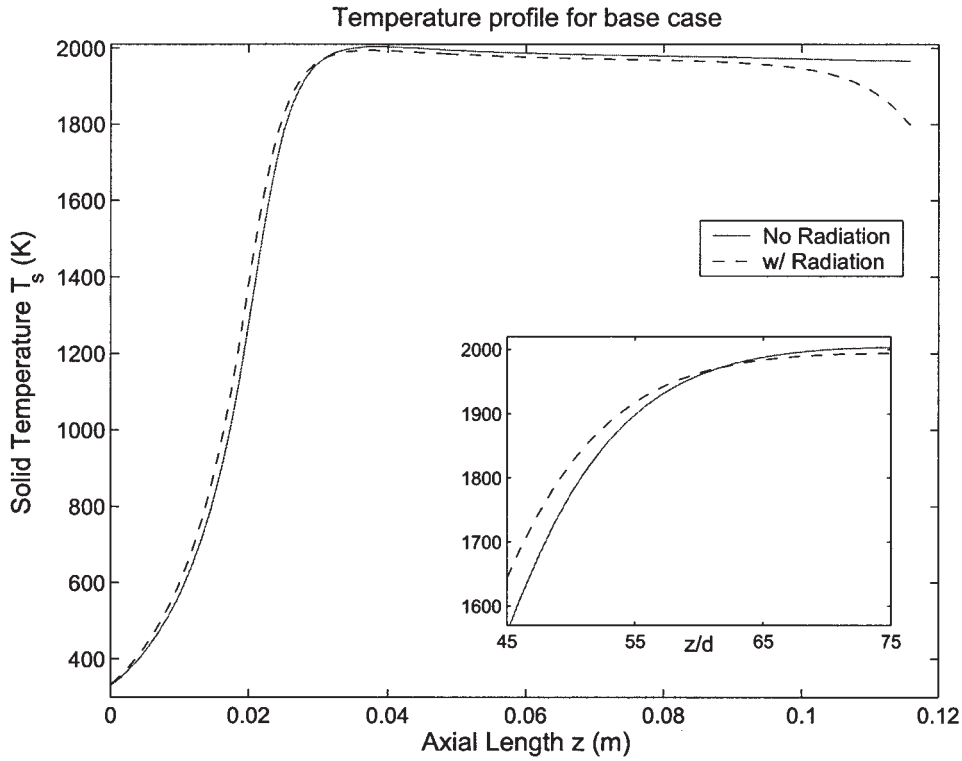

Figure 4. Effect of radiation on solid temperature.

The temperature profile shifts upstream by two diameters (inset: zoomed-in at temperature peak, dimensionless length *z/d* is the abscissa). Radiation loss at the reactor end causes a drop in temperature. Concentration profiles (not shown) are almost same in both cases.

at the outlet as a result of radiation. However, in contrast to the previous case, the temperature drop at the reactor end caused a significant decrease in hydrogen yield in the shorter reactor. The decrease in the hydrogen yield was about 2–3%. We also found that changing the emissivity resulted in temperature and concentration profiles similar to those obtained with $\varepsilon = 0.8$. Thus, one can use the black body assumption to reduce the computational burden in calculating the radiation flux, with only negligible increases in error. All these results are consistent with those reported in the literature.[20,21]

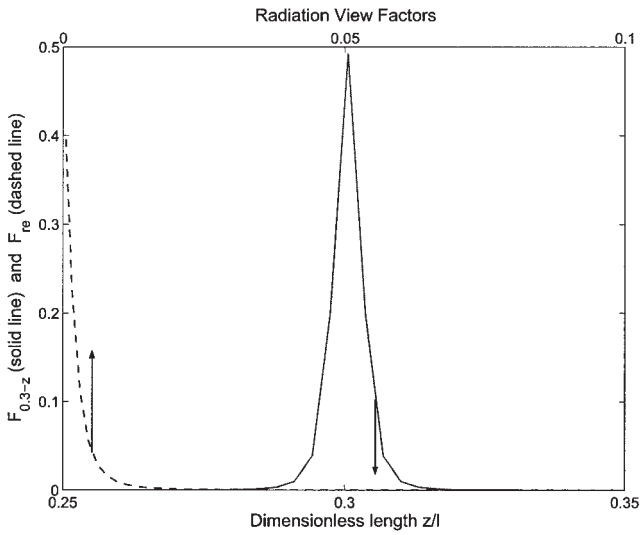

Figure 5. Ring–ring (solid line, bottom abscissa) and ring–end (dashed line, top abscissa) view factors as a function of the dimensionless axial coordinate.

The view factors diminish rapidly with the axial distance.

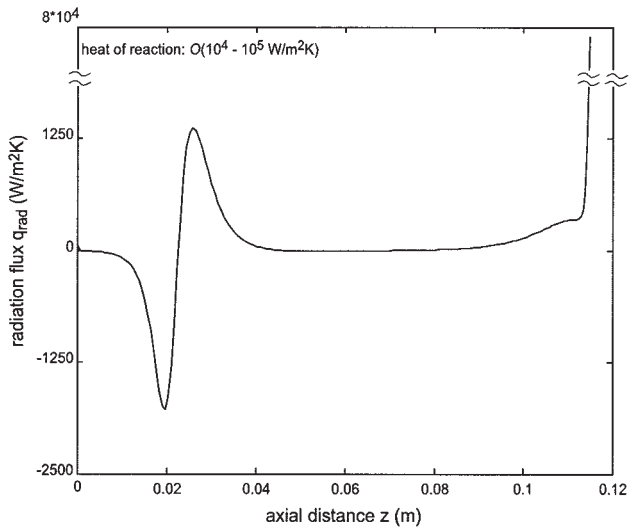

Figure 6. Radiation flux at steady state within the reactor.

Except at the reactor end, radiation flux is 1 to 2 orders of magnitude lower than convection or reaction heat fluxes.

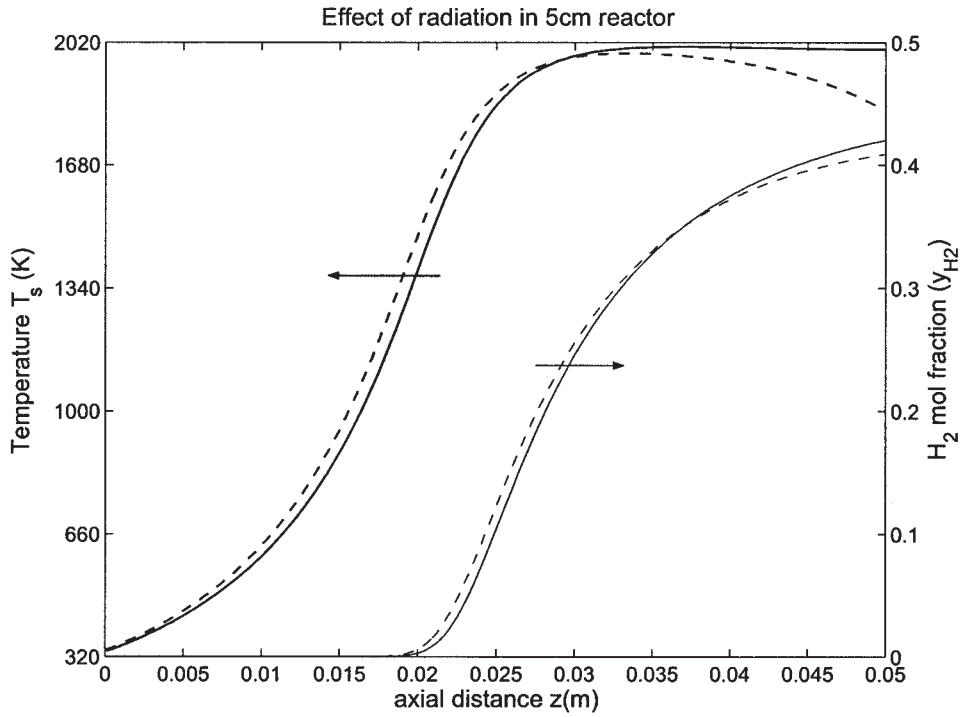

Figure 7. Effect of radiation in a 5-cm reactor.

Thick lines, T_s; thin lines, y_{H_2}; solid line, without radiation; dashed line, with radiation. Temperature drop at the reactor end causes a decrease in H_2 yield.

Conclusions

A 1-D model for simulation of autothermal partial oxidation of methane in a microreactor with unidirectional (UD) and reverse-flow (RF) modes of operation was developed. Two different kinetic models for methane oxidation and reforming from the literature were compared; an analysis of timescales of the individual processes occurring in the reactor was presented; and the effect of radiative heat transfer on the reactor performance was analyzed. Specific results of this work include:

- The reaction kinetics presented by Gosiewski et al.[7] (GOS model) and de Smet et al.[8] (NK model) were compared. The GOS model was able to reproduce the experimental results reported by Kikas et al.[5] A maximum improvement of 4.2% in hydrogen yield was predicted for the RF operation compared to the UD operation. The NK model, on the other hand, did not show any improvement in the reactor performance for the RF operation.
- An analysis of timescales of individual processes occurring within the reactor was presented. The timescale of diffusion was lower than that of reactions. Thus, the reactions occurred at their intrinsic rates.
- Based on the timescales, the species concentrations were found to be under quasi-steady state and the overall thermal dynamics of the reactor critical in defining the reactor operation in the UD or RF operation.
- Radiation heat transfer did not have a significant impact on the performance of the longer reactor. Consistent with the published literature,[20,21] radiation resulted in a one to two diameter shift in the temperature profile and a sharp drop in the temperature at the reactor exit. However, because of the large aspect ratio ($l/d = 232$) in the reactor, the overall effect was insignificant.
- In contrast to this, the hydrogen yield in a shorter reactor (aspect ratio $l/d = 100$) with radiation included was about 2% lower than that without radiation.

Acknowledgments

The authors gratefully acknowledge Dr. Athanasios Nenes in the School of Chemical and Biomolecular Engineering for help with the numerical simulations. J.H.L. gratefully acknowledges the financial support from NSF (CTS-0301993). A.G.F. gratefully acknowledges a NASA grant (UG03-0050 NRA 02-OBPR-03, Project Monitor Dr. Karen Weiland) to support this work.

Notation

$\underline{a}$ = surface area per unit volume of solid, m^2/m_s^3
$\hat{a}$ = surface area per unit void volume, m^2/m_g^3
c_{pg} = average specific heat of the gas, J kg^{-1} K^{-1}
c_s = specific heat of solid, J kg^{-1} K^{-1}
C = concentration, mol/m^3
D_{im} = diffusivity, m^2/s
E = activation energy, J/mol
E_b = Blackbody emissive power (W/m^2)
F = radiation view factor
h_v = heat-transfer coefficient, W m^{-2} K^{-1}
k = Arrhenius rate constant, $(mol/m^3)^{-\iota}$ s^{-1}
k_{gi} = mass transfer coefficient, m/s
l = reactor length, m
M_i = molecular weight, kmol/kg
n_{rxn} = number of reactions
n_{sp} = number of species
p = pressure, bar
q_r = radiation heat flux, W m^{-2} K^{-1}

r = reaction rate, mol $m_{surface}^{-2}$ s^{-1}
R = gas constant, J mol^{-1} K^{-1}
t = time, s
T = temperature, K
v = gas velocity, m/s
ΔH = heat of reaction, J/mol
z = axial coordinate, m

Greek letters

α = coefficient to split reaction heat between gas and solid
ε = emissivity of the reactor wall
λ = thermal conductivity, W m^{-1} K^{-1}
ν = stoichiometric coefficient
ϕ = any state variable, units vary
ρ = density, kg/m^3
σ = Stefan-Boltzmann constant = 5.67×10^{-8} $W/m^2/K^4$
τ = time scale, s

Subscripts and superscripts

0 = condition at reactor inlet
i = ith species
j = jth reaction
g = gas phase
s = solid surface

Literature Cited

1. Baa X, Iglesia E, Xu Y, eds. Natural gas conversion. Vol. VII. *Studies in Surface Science and Catalysis*. Dalian, China: Elsevier; 2004. [Also see the Proceedings of the previous Natural Gas Conversion Symposia. References are available from de Smet et al.[8]]
2. For example, see http://www.fischer-tropsch.org/ and documents and references therein.
3. Stranges AN. The U.S. Bureau of Mines Synthetic Liquid Fuels Programme, 1920–1950s: German connections and american advances. *Ann Sci*. 1997;54:29-68.
4. Hirschenhofer JH, Stauffer DB, Engleman RR, Klett MG. *Fuel Cell Handbook*. DOE/FETC-99/1076, for DS DOE 4th Edition. Reading, PA: Parsons Corporation; 1998.
5. Kikas T, Bardenshteyn I, Williamson C, Ejimofor C, Puri P, Fedorov AG. Hydrogen production in a reverse-flow autothermal catalytic microreactor: From evidence of performance enhancement to innovative reactor design. *Ind Eng Chem Res*. 2003;42:6273-6279.
6. Hickman DA, Schmidt LD. Production of syngas by direct catalytic oxidation of methane. *Science*. 1993;259:343-346.
7. Gosiewski K, Bartmann D, Moszczynski M, Mleczko L. Effect of the intraparticle mass transport limitations on temperature profiles and catalytic performance of the reverse-flow reactor for the partial oxidation of methane to synthesis gas. *Chem Eng Sci*. 1999;54:4589-4602.
8. de Smet CRH, de Croon MHJM, Berger RJ, Marin GB, Schouten JC. Design of adiabatic fixed-bed reactors for the partial oxidation of methane to synthesis gas. Application to production of methanol and hydrogen-for-fuel-cells. *Chem Eng Sci*. 2001;56:4849-4861.
9. Blanks RF, Wittrig TS, Peterson DA. Bidirectional adiabatic synthesis gas generator. *Chem Eng Sci*. 1990;45:2407-2413.
10. de Groote AM, Froment GF, Kobylinski TH. Synthesis gas production from natural gas in a fixed bed reactor with reversed flow. *Can J Chem Eng*. 1996;74:735-742.
11. Kaisare NS, Lee JH, Fedorov AG. Hydrogen generation in a reverse-flow microreactor: 2. Simulation and analysis. *AIChE J*. 2005;51;000-000.
12. Xu J, Froment GF. Methane steam reforming, methanation and water-gas shift: I. Intrinsic kinetics. *AIChE J*. 1989;35:88-96.
13. Numaguchi T, Kikuchi K. Intrinsic kinetics and design simulation in a complex reaction network: Steam-methane reforming. *Chem Eng Sci*. 1988;43:2295-2301.
14. Trimm DL, Lam C-W. The combustion of methane on platinum-alumina fibre catalysts—I. *Chem Eng Sci*. 1980;35:1405-1413.
15. Brown PN, Hindmarsh AC, Petzold LR. Consistent initial condition calculation for differential–algebraic systems. Report UCRL-JC-122175. University of California (for the U.S. Department of Energy). Livermore, CA: Lawrence Livermore National Laboratory; 1995.
16. Varma A, Morbidelli M. *Mathematical Methods in Chemical Engineering*. New York, NY: Oxford Univ. Press; 1997.
17. Rankin AJ, Hayes RE, Kolaczkowski ST. Annular flow in a catalytic monolith reactor: The significance of centerline probe temperatures. *Trans IChemE Part A*. 1995;73:110-121.
18. Matros YS. *Unsteady Processes in Catalytic Reactors* (Studies in Surface Science and Catalysis series). Amsterdam: Elsevier; 1985.
19. Modest MF. *Radiative Heat Transfer*. New York, NY: McGraw-Hill; 1993.
20. Boehman A. Radiation heat transfer in catalytic monoliths. *AIChE J*. 1998;44:2745-2755.
21. Fu X, Viskanta R, Gore JP. Combustion and heat transfer interaction in a pore-scale refractory tube burner. *J Thermophys Heat Transfer*. 1998;12:164-171.

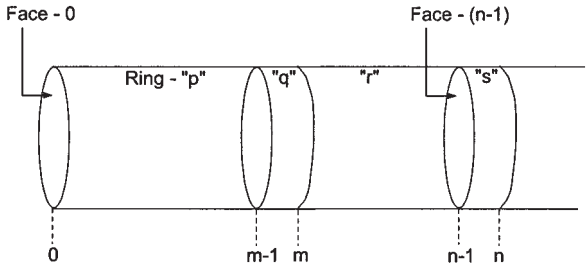

Figure A1. Surfaces considered for view factor calculation.

Appendix: Finite Area View Factors

Consider two ring elements at locations m and n as shown in Figure A1. Let z_m represent the distance from the left end of the channel to the right boundary of mth grid and Δz_m represent the axial extent of the grid element (that is, $\Delta z_m = z_m - z_{m-1}$). Let p, q, r, and s represent the cylindrical surfaces and 0, $m-1$, m, $n-1$, and n represent the faces.

The dimensionless lengths are defined as

$$X_n = \frac{z_n}{d} \qquad \Delta X_n = \frac{\Delta z_n}{d}$$

The cross-sectional areas are $A_0 = A_m = A_n = \pi d^2/4$ and the ring surface area is $A_s = \pi d \Delta z_n$. Thus, the ratio of areas is

$$\frac{A_0}{A_s} = \frac{1}{\Delta X_n} \tag{A1}$$

The view factors satisfy the following equations

$$\text{For an enclosure } \sum_j F_{i-j} = 1 \qquad A_i F_{i-j} = A_j F_{j-i}$$

The above equations are known as the "summation rule" and the "reciprocity rule," respectively.[19]

Finally, the view factor between two parallel coaxial disks of radii r separated by a distance z is given by[19]

$$G = 0.5(\xi - \sqrt{\xi^2 - 4}) \tag{A2}$$

where G represents the end–end view factor, and $\xi = 2 + (z/r)^2 = 2 + 4X^2$. Thus,

$$G_{i-j} = 1 + 2(X_i - X_j)^2 - 2\sqrt{(X_i - X_j)^4 + (X_i - X_j)^2} \tag{A3}$$

Ring–end view factor

We seek to obtain $F_{re}(z_n) \triangleq F_{s-0}$. We note the reciprocity rule

$$F_{s-0} = \frac{A_0}{A_s} F_{0-s} \tag{A4}$$

The summation rules for cylindrical enclosures from z_0 to z_n, and that from z_0 to z_{n-1} are given as

$$\begin{aligned} F_{0-(pqr)} + F_{0-s} + G_{0-n} &= 1 \\ \underline{F_{0-(pqr)} + G_{0-(n-1)} = 1} & \end{aligned} \tag{A5}$$

$$F_{0-s} = G_{0-(n-1)} - G_{0-n} \tag{A6}$$

Using the reciprocity rule (Eq. A4), we obtain

$$F_{re}(z_n) = \frac{1}{2\Delta X_n}\left[\sqrt{X_n^4 + X_n^2} - \sqrt{X_{n-1}^4 + X_{n-1}^2} + X_{n-1}^2 - X_n^2\right] \tag{A7}$$

View factor from ring to itself

To find the view factor for the nth ring to itself, we use the summation rule for the enclosure formed by the ring s and its faces $n - 1$ and n

$$F_{s-(n-1)} + F_{s-s} + F_{s-n} = 1 \tag{A8}$$

We note that because of the symmetry, $F_{s-(n-1)} = F_{s-n}$. They represent the view factor from a ring element to one of its faces. Equation A7 represents the view factor from the ring to face located at $z = 0$. The view factor from the ring to face located at z_{n-1} is just $F_{re}(|z_n - z_{n-1}|)$ (that is, in Eq. A7, replace X_n with ΔX_n and X_{n-1} with 0). Through straightforward manipulations, one can verify that

$$F_{n-n} \triangleq F_{s-s} = 1 + \Delta X_n - \sqrt{\Delta X_n^2 + 1} \tag{A9}$$

Ring–Ring View Factor

To obtain the ring–ring view factor $F_{n-m} \triangleq F_{s-q}$, we apply the summation rule to the cylindrical enclosures from z_{m-1} to z_n and from z_m to z_n

$$F_{s-n} + F_{s-s} + F_{s-r} + F_{s-q} + F_{s-(m-1)} = 1 \tag{A10}$$

$$F_{s-n} + F_{s-s} + F_{s-r} + F_{s-m} = 1 \tag{A11}$$

Subtracting the two and rearranging, we obtain

$$F_{s-q} = F_{re}(|z_n - z_m|) - F_{re}(|z_n - z_{m-1}|) \tag{A12}$$

From Eq. A7, for $i = m - 1$, m

$$F_{re}(|z_n - z_i|) = \frac{1}{2\Delta X_n}\left[(X_{n-1} - X_i)^2 - (X_n - X_i)^2 + \Xi_{n-i} - \Xi_{(n-1)-i}\right] \tag{A13}$$

where

$$\Xi_{i-j} \triangleq \sqrt{(X_i - X_j)^4 + (X_i - X_j)^2} \tag{A14}$$

After straightforward manipulations, we obtain the ring–ring view factor

$$F_{n-m} = \frac{1}{2\Delta X_n}\left[2\Delta X_m \Delta X_n + \Xi_{n-m} + \Xi_{(n-1)-(m-1)} - \Xi_{(n-1)-m} - \Xi_{n-(m-1)}\right] \tag{A15}$$

Manuscript received Aug. 24, 2004, and revision received Dec. 9, 2004.